Optical response in the excitonic insulating state: Variational cluster approach

Hengyue Li* and Junya Otsuki†
Department of Physics, Tohoku University, Sendai 980-8578, Japan

Makoto Naka
Waseda Institute for Advanced Study, Waseda University, Tokyo 169-8050, Japan

Sumio Ishihara
Department of Physics, Tohoku University, Sendai 980-8578, Japan

(Received 18 November 2019; revised manuscript received 3 March 2020; accepted 5 March 2020; published 19 March 2020)

Optical responses in an excitonic insulating (EI) system with strong electron correlation are studied. We adopt the two-orbital Hubbard model with a finite energy difference between the two orbitals where the spin state degree of freedom exists. This model is analyzed by the variational cluster approach. In order to include the local electron correlation effect, the vertex correction is taken into account in the formulation of the optical conductivity spectra. We calculate a finite-temperature phase diagram in which an EI phase appears between a low-spin band insulating state and a high-spin Mott insulating state. Characteristic components of the optical conductivity spectra consisting of a sharp peak and continuum appear in the EI phase. Integrated intensity almost follows the order parameter of the EI state, suggesting that this component is available to identify the EI phases and transitions.

DOI: 10.1103/PhysRevB.101.125117

I. INTRODUCTION

The excitonic insulating (EI) state was proposed more than a half century ago in semiconductors and semimetals and has been studied intensively on both the experimental and theoretical sides [1–4]. When the attractive Coulomb interaction between electrons and holes overcomes the insulating gap energy, the electron-hole pairs are produced spontaneously, and a macroscopic number of excitons are condensed in low temperatures. Some conceptual similarities of this excitonic condensation to the superconductivity and the charge-density wave have been examined. Owing to recent great progress in the experimental technique, the study of the EI state has been revived. Prototypical examples are $1T$-$TiSe_2$ [5] and $TaNiSe_5$ [6], in which flattenings of the top of the valence band dispersions were observed below the structural-phase transition temperatures by angle-resolved photoemission spectroscopy (ARPES).

Another candidate material for the EI state is the cobalt oxides with the perovskite crystal structure, $R_{1-x}A_xCoO_3$, where R and A are a rare-earth ion and an alkaline-earth ion, respectively. This series of materials is widely recognized to show the spin crossover phenomena by changing temperature, pressure, and magnetic field [7,8]. In a single Co^{3+}, three kinds of electron configurations are possible: $(t_{2g})^6(e_g)^0$ with $S = 0$, $(t_{2g})^5(e_g)^1$ with $S = 1$, and $(t_{2g})^4(e_g)^2$ with $S = 2$, which are termed the low-spin (LS), intermediate-spin, and high-spin (HS) states, respectively. The stability of the three spin states is governed dominantly by the competition of the crystalline field splitting and Hund's coupling. Recently, an EI state was proposed in $Pr_{1-x}Ca_xCoO_3$, where a metal-insulator transition was observed around 90 K by the magnetization, the specific heat, and the structural analyses [9,10]. Because of the lack of evidence of the charge and/or orbital orders so far, an EI state is considered to be a possible origin of this transition. An EI state was also proposed in $LaCoO_3$ under a high magnetic field around 100 T [11]. A number of theoretical examinations were performed to clarify the EI state in the perovskite cobalites and the relation to the spin-state degree of freedom in the Co ions [12–15].

One of the unresolved issues in the EI research is to develop an experimental way to identify the EI state and transition. The flattening of the top of the valence band dispersion observed by ARPES suggests the EI transition, although this is not the direct evidence of the EI transition. Photoinduced transient dynamics provide rich information about the driving force of the structural phase transition by utilizing different timescales of the electronic and lattice degrees of freedom [16–18]. Once the direct method to identify the EI phase is settled, this technique will be applied to a wide range of candidate materials.

In this paper, we study the optical responses in EI states. The two-orbital Hubbard model with a finite energy difference between the orbitals is analyzed by utilizing the variational cluster approach. The optical conductivity spectra are formulated in the two-particle Green's function, in which the vertex corrections are taken into account. The finite-temperature T

*Present address: Fujitsu R&D Center, Beijing 100025, China.
†Present address: Research Institute for Interdisciplinary Science, Okayama University, Okayama 700-8530, Japan.

phase diagram and the one-particle excitation spectra are obtained in the EI phase. A characteristic structure in the optical conductivity spectra emerges in the EI state due to the hybridization between the two orbitals. The intensity of this structure at low temperatures almost follows the EI order parameter. We propose that this is available to identify the EI state.

In Sec. II, the adopted two-orbital Hubbard model with the finite energy difference is introduced. The variational-cluster approach (VCA) applied to the model is introduced in Sec. III A, and the formulation of the optical conductivity spectra with the vertex correction is explained in Sec. III B. The numerical results of the finite-T phase diagram and the excitation spectra are presented in Sec. IV. Section V is devoted to concluding remarks.

II. MODEL

We start from the two-orbital Hubbard model with the finite energy difference between the two orbitals given by

$$H = H_L + H_t, \tag{1}$$

where H_L represents the local part and H_t represents the electron hoppings between different sites. The first term is given by

$$H_L = \sum_i [h_0(i) + h_{\rm int}(i)], \tag{2}$$

with

$$h_0(i) = \frac{D}{2}\sum_\sigma (n_{ia\sigma} - n_{ib\sigma}) - \mu \sum_{\alpha\sigma} n_{i\alpha\sigma}, \tag{3}$$

$$h_{\rm int}(i) = U\sum_\alpha n_{i\alpha\uparrow}n_{i\alpha\downarrow} + V n_{ia}n_{ib} + J\sum_{\sigma\sigma'} c^\dagger_{ia\sigma}c^\dagger_{ib\sigma'}c_{ia\sigma'}c_{ib\sigma} + I\sum_\alpha c^\dagger_{i\alpha\uparrow}c^\dagger_{i\alpha\downarrow}c_{i\bar\alpha\downarrow}c_{i\bar\alpha\uparrow}. \tag{4}$$

We introduce the creation (annihilation) operator $c^\dagger_{i\alpha\sigma}$ ($c_{i\alpha\sigma}$) of an electron with spin σ ($=\uparrow,\downarrow$) and orbital α ($=a,b$) at site i, the number operator $n_{i\alpha} = \sum_\sigma n_{i\alpha\sigma} = \sum_\sigma c^\dagger_{i\alpha\sigma}c_{i\alpha\sigma}$, and $\bar\alpha = a$ (b) for $\alpha = b$ (a). D is the energy difference between orbitals a and b, U and V are the intra- and interorbital Coulomb interactions, respectively, J is the Hund's coupling, I is the pair hopping, and μ is the chemical potential. The second term in Eq. (1) is given as

$$H_t = \sum_{\langle ij\rangle} h_t(i,j), \tag{5}$$

with

$$h_t(i,j) = \sum_{\alpha\sigma} t_\alpha c^\dagger_{i\alpha\sigma}c_{j\alpha\sigma} \tag{6}$$

for the nearest-neighbor (NN) sites, where t_α represents the hopping integral inside orbital α. The hopping integrals are assumed to be diagonal with respect to the orbital. The present Hamiltonian is schematically shown in Fig. 1.

In numerical calculations, we consider a two-dimensional square lattice with the number of sites N. We take the limit $N\to\infty$ and replace summations over momentum with integrals, which can be computed numerically. The two hopping integrals are assumed to be equal to each other and are used as the energy unit, $t \equiv t_a = t_b = 1$. The bandwidth becomes $W = 8$. The orbital splitting D is set to $D = 9$ so that the noninteracting band forms an insulator with a small energy gap. We fix V and I using the relations in the atomic limit, $V = U - 2J$ and $I = J$. Then, we vary the value of J, keeping $U = 5J$. The electron number is fixed to be half filling by $\mu = (U + 2V - J)/2$, which satisfies the particle-hole symmetry in the system.

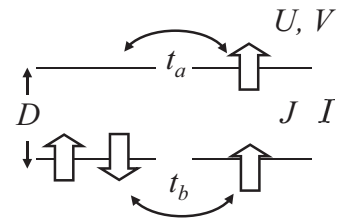

FIG. 1. A schematic illustration of the Hamiltonian in Eq. (1). Horizontal bars and block arrows represent the two orbitals and the electron spins, respectively.

III. METHOD

In order to examine electronic structures in various phases emerging due to local electronic correlations, we employ the VCA developed by Potthoff *et al.* [19]. In this section, we present an introduction to the VCA and its application to the present model. We also present the method to calculate the optical conductivity where the vertex correction is taken into account.

A. A brief introduction to the VCA

The VCA is a general framework of cluster theories, which includes the cluster perturbation theory (CPT) [19,20] and the cluster extension of the dynamical mean-field theory [21–23] depending on the number of uncorrelated "bath" sites (zero for the former and infinity for the latter) [19]. In the case without bath sites, the VCA forms a generalization of the CPT where we can introduce local potentials as a variational parameter, which allows us to address symmetry-broken phases. This special case is called variational CPT (V-CPT) [24]. The VCA, in particular, V-CPT, has been successfully applied to many systems such as the antiferromagnetic (AF) phase [24], charge ordering [25], high-T_c cuprates [26], spin liquids [27], correlated topological insulators [28], bosonic systems and Bose-Einstein condensation [29–31], and nonequilibrium systems [32,33]. Detailed explanations of the method can be found in Refs. [19,24,25,34–37]. In the following, we give a brief summary of the method.

The VCA is formulated based on the self-energy functional theory (SFT) [34,35]. In the SFT, we consider the self-energy functional of the thermodynamic potential $\Omega[\mathbf{\Sigma}]$, which is given by

$$\Omega[\mathbf{\Sigma}] = \mathcal{F}_U[\mathbf{\Sigma}] - \sum_{\boldsymbol{k}} {\rm Tr}\ln\left\{-\left[\mathcal{G}_0^{-1}(\boldsymbol{k}) - \mathbf{\Sigma}\right]^{-1}\right\}, \tag{7}$$

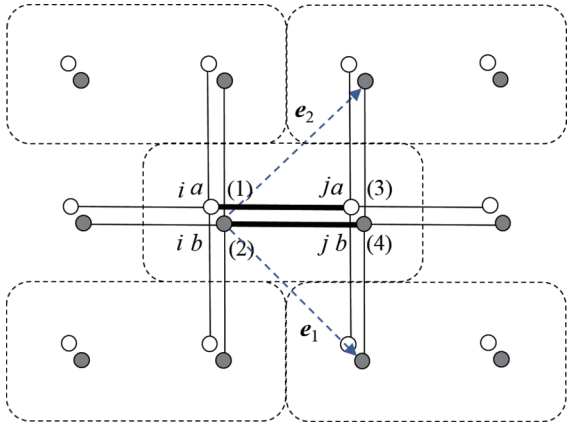

FIG. 2. The present reference system. Dashed rectangles represent unit cells. Open and solid circles represent orbitals a and b, respectively. Labels (1)–(4) indicate the independent orbitals and sites in a cluster.

where $\mathcal{F}_U[\boldsymbol{\Sigma}]$ is the Legendre transform of the Luttinger-Ward functional $\Phi[\boldsymbol{\mathcal{G}}]$ [38], $\boldsymbol{G}_0$ ($\boldsymbol{\mathcal{G}}$) is the noninteracting (interacting) Green's function, $\boldsymbol{\Sigma}$ is the trial self-energy, and $\boldsymbol{k}$ is the wave vector in the Brillouin zone. The bold symbols, $\boldsymbol{\Sigma}$ and $\boldsymbol{\mathcal{G}}_0$, represent matrices with the spin and orbital indices, and Tr stands for summations over these indices and the Matsubara frequencies: $\mathrm{Tr} \equiv T\sum_{\omega_n}\sum_{\alpha\sigma}$. The subscript U in $\mathcal{F}_U$ indicates that $\mathcal{F}_U$ depends only on the two-body (interaction) terms and not on the one-body terms. According to the SFT [34,35], the functional $\Omega[\boldsymbol{\Sigma}]$ holds the variational principle with respect to $\boldsymbol{\Sigma}$, $\delta\Omega[\boldsymbol{\Sigma}]/\delta\boldsymbol{\Sigma} = 0$, as in the Luttinger-Ward formalism in terms of $\boldsymbol{\mathcal{G}}$ [38]. In other words, our task is to find the stationary point of Eq. (7) rather than to solve the original model directly.

The functional $\mathcal{F}_U[\boldsymbol{\Sigma}]$ takes into account interactions but is essentially impossible to evaluate exactly for the arbitrary form of $\boldsymbol{\Sigma}$. In the VCA, we instead evaluate $\mathcal{F}_U[\boldsymbol{\Sigma}]$ using an auxiliary cluster model called the "reference" system. The Hamiltonian H' of the reference system is given by the form

$$H' = H_L + H'_t, \tag{8}$$

where H'_t contains arbitrary one-body terms (hopping and local potential). In particular, we can consider a situation where some hopping integrals are absent so that the lattice is divided into clusters which are arranged periodically (see Fig. 2). When the cluster is small enough, we can diagonalize H' and evaluate physical quantities such as the thermodynamic potential Ω' and the Green's function $\boldsymbol{G}'$ in the reference system. Furthermore, H'_t can include any potentials that break the symmetries of the original Hamiltonian, leading to a description of the symmetry-broken states.

The important point in Eq. (8) is that the interaction H_L is the same as in H. This means that the functional $\mathcal{F}_U[\boldsymbol{\Sigma}]$ is common between the original and reference systems. Therefore, we can eliminate $\mathcal{F}_U[\boldsymbol{\Sigma}]$ from the equations for Ω and Ω' and obtain

$$\Omega[\boldsymbol{\Sigma}] = \Omega'[\boldsymbol{\Sigma}] - \sum_{\boldsymbol{q}} \mathrm{Tr}\ln(\mathbf{1} - \boldsymbol{V}_{\boldsymbol{q}}\boldsymbol{G}'), \tag{9}$$

where $\boldsymbol{q}$ is the reduced wave vector, when the cluster contains more than one site, and $\boldsymbol{V}_{\boldsymbol{q}} = \boldsymbol{G}_0'^{-1} - \boldsymbol{\mathcal{G}}_0^{-1}(\boldsymbol{q})$ is the difference of the signal-particle terms between the original system and the reference system.

All quantities on the right-hand side of Eq. (9) can be computed numerically with use of the reference system, meaning that we can evaluate $\Omega[\boldsymbol{\Sigma}]$ *exactly*. However, the argument $\boldsymbol{\Sigma}$ cannot be changed arbitrarily and is determined only through one-body parameters in H'_t, namely, $\boldsymbol{\Sigma} = \boldsymbol{\Sigma}(t')$, where t' indicates a parameter in H'_t. We will search for the stationary point of $\Omega[\boldsymbol{\Sigma}]$ within this *restricted* space of $\boldsymbol{\Sigma}(t')$ by $\partial\Omega[\boldsymbol{\Sigma}(t')]/\partial t' = 0$.

B. Reference system

For the reference system, we make a minimal choice that is required for discussing staggered ordered states. We retain hopping only between a pair of sites so that two-site clusters are isolated, as shown in Fig. 2. The one-body part H'_t in the Hamiltonian, Eq. (8), now reads

$$H'_t = \sum_R \left[\sum_{i,j\in R} h_t(i,j) + \sum_{i\in R} h_\Delta(i) \right], \tag{10}$$

where $\boldsymbol{R}$ is the index which specifies clusters. The second term, $h_\Delta(i)$, is introduced to represent symmetry-breaking local potentials, which will be discussed in Sec. III C.

It is convenient to introduce a combined site-orbital index, $(i,\alpha) \equiv l = 1,\ldots,4(\equiv L)$, in each cluster (see Fig. 2) and define an L-dimensional vector $\psi_{\boldsymbol{R}\sigma}$ of annihilation or creation operators such as $\psi_{\boldsymbol{R}\sigma} = (c_{1\sigma},\ldots,c_{L\sigma})^{\mathrm{T}}$. Using this representation, H' in Eq. (8) is represented as

$$H' = \sum_{\boldsymbol{R}\sigma} \psi^\dagger_{\boldsymbol{R}\sigma}(\boldsymbol{\mathcal{H}} + \boldsymbol{\Delta}^\sigma)\psi_{\boldsymbol{R}\sigma} + \sum_i h_{\mathrm{int}}(i), \tag{11}$$

where $\boldsymbol{\mathcal{H}}$ and $\boldsymbol{\Delta}^\sigma$ denote the matrix elements of the one-body part, $h_t(i,j) + h_{L0}(i)$ and $h_\Delta(i)$, respectively. The explicit expression of $\boldsymbol{\mathcal{H}}$ is given by

$$\boldsymbol{\mathcal{H}} = \begin{pmatrix} \frac{D}{2} - \mu & 0 & t_a & 0 \\ 0 & -\frac{D}{2} - \mu & 0 & t_b \\ t_a & 0 & \frac{D}{2} - \mu & 0 \\ 0 & t_b & 0 & -\frac{D}{2} - \mu \end{pmatrix}. \tag{12}$$

Including h_{int}, we diagonalize H' by means of the exact diagonalization method and compute $\boldsymbol{G}'(\omega)$.

In order to calculate Ω in Eq. (9), we further need the expression of $\boldsymbol{V}_{\boldsymbol{q}} = \boldsymbol{G}_0'^{-1} - \boldsymbol{\mathcal{G}}_0^{-1}(\boldsymbol{q})$, which represents the difference of the noninteracting Hamiltonians in the reference and original systems, i.e., $H - H'$. More precisely, its bilinear form, $H - H' = \sum_{\boldsymbol{R}\sigma} \psi^\dagger_{\boldsymbol{R}\sigma}\boldsymbol{V}^\sigma_{\boldsymbol{q}}\psi_{\boldsymbol{R}\sigma}$, yields the representation for $\boldsymbol{V}^\sigma_{\boldsymbol{q}}$ (which depends on σ because of $\boldsymbol{\Delta}^\sigma$). We thus obtain

$$\boldsymbol{V}^\sigma_{\boldsymbol{q}} = \boldsymbol{\mathcal{T}}_{\boldsymbol{q}} - \boldsymbol{\Delta}^\sigma, \tag{13}$$

where $\mathcal{T}_{\boldsymbol{q}}$ denotes hopping, which connects different clusters. Its explicit expression is given by

$$\mathcal{T}_{\boldsymbol{q}} = \begin{pmatrix} 0 & 0 & t_a E_{\boldsymbol{q}} & 0 \\ 0 & 0 & 0 & t_b E_{\boldsymbol{q}} \\ t_a E_{\boldsymbol{q}}^* & 0 & 0 & 0 \\ 0 & t_b E_{\boldsymbol{q}}^* & 0 & 0 \end{pmatrix}, \tag{14}$$

where $E_{\boldsymbol{q}} = e^{i\boldsymbol{q}\cdot\boldsymbol{e}_1} + e^{i\boldsymbol{q}\cdot\boldsymbol{e}_2} + e^{i\boldsymbol{q}\cdot(\boldsymbol{e}_1+\boldsymbol{e}_2)}$, with $\boldsymbol{e}_1$ and $\boldsymbol{e}_2$ being the bases of the superlattice as shown in Fig. 2.

C. Order parameters

In the present study, we consider three kinds of long-range orders: the AF state [24], the EI state [39,40], and the HS-LS ordered (HL) state [14,15]. Accordingly, we define three Weiss fields given by

$$H_\Delta \equiv \sum_i h_\Delta(i) = \sum_O \delta_O p_O, \tag{15}$$

where O is either AF, EI, or HL. The potential δ_O is a real number to be determined by the variational principle, and the operator p_O is defined by

$$p_{\mathrm{AF}} = \sum_{i\alpha} (-1)^i (n_{i\alpha\uparrow} - n_{i\alpha\downarrow}), \tag{16}$$

$$p_{\mathrm{EI}} = \sum_{i\sigma} e^{i\boldsymbol{Q}\cdot\boldsymbol{r}_i} (-1)^\sigma (c^\dagger_{ia\sigma} c_{ib\sigma} + \mathrm{H.c.}), \tag{17}$$

$$p_{\mathrm{HL}} = \sum_{i\alpha\sigma} e^{i\boldsymbol{Q}\cdot\boldsymbol{r}_i} (-1)^\alpha c^\dagger_{i\alpha\sigma} c_{i\alpha\sigma}, \tag{18}$$

with $\boldsymbol{Q} = (\pi, \pi)$. We note that p_{AF} and p_{EI} imply the staggered Néel order and the excitonic order, respectively, and p_{HL} represents the spatial alignment of the HS and LS states.

By transforming H_Δ into the L-dimensional vector representation, $H_\Delta = \sum_{\boldsymbol{R}\sigma} \psi^\dagger_{\boldsymbol{R}\sigma} \boldsymbol{\Delta}^\sigma \psi_{\boldsymbol{R}\sigma}$, we obtain the expression of $\boldsymbol{\Delta}^\sigma$ as

$$\boldsymbol{\Delta}^\sigma = \sum_O \delta_O \boldsymbol{\Delta}^\sigma_O, \tag{19}$$

with

$$\boldsymbol{\Delta}^\sigma_{\mathrm{AF}} = \sigma \begin{pmatrix} 1 & 0 & 0 & 0 \\ 0 & 1 & 0 & 0 \\ 0 & 0 & -1 & 0 \\ 0 & 0 & 0 & -1 \end{pmatrix}, \tag{20}$$

$$\boldsymbol{\Delta}^\sigma_{\mathrm{EI}} = \sigma \begin{pmatrix} 0 & 1 & 0 & 0 \\ 0 & 0 & 0 & 0 \\ 1 & 0 & 0 & -1 \\ 0 & 0 & -1 & 0 \end{pmatrix}, \tag{21}$$

$$\boldsymbol{\Delta}^\sigma_{\mathrm{HL}} = \begin{pmatrix} 1 & 0 & 0 & 0 \\ 0 & -1 & 0 & 0 \\ 0 & 0 & -1 & 0 \\ 0 & 0 & 0 & 1 \end{pmatrix}. \tag{22}$$

We thus have all ingredients for evaluation of Ω in Eq. (9).

D. Computation procedure

With the expressions above, the variational principle is represented as $\partial\Omega/\partial\delta_O = 0$ for each field δ_O. We summarize below the standard steps for the VCA calculation:

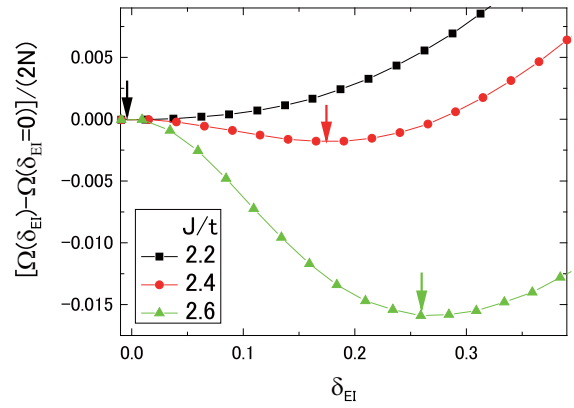

FIG. 3. The ground potential $\Omega/2N$ as a function of the potential for the EI order δ_{EI} for various values of J/t. The arrows indicate the stationary points. We set $T/t = 0.1$.

(i) For trial values of δ_O, we solve the reference system whose Hamiltonian H' is given by Eq. (11) and compute $\boldsymbol{G}'(\omega)$ and Ω'.

(ii) We calculate Ω in the lattice system using Eqs. (9) and (13).

(iii) We repeat the above steps by varying the values of δ_O to find the stationary point of Ω. Thus, the physical self-energy $\boldsymbol{\Sigma}$ is obtained.

(iv) At the stationary point, using the self-energy $\boldsymbol{\Sigma}$ in the reference system, we calculate the lattice Green's function by $\boldsymbol{G}(\boldsymbol{q},\omega) = [\boldsymbol{\mathcal{G}}_0^{-1}(\boldsymbol{q},\omega) - \boldsymbol{\Sigma}(\omega)]^{-1}$ and other physical quantities.

To illustrate step (iii), we show numerical results for $\Omega/2N$ as a function of δ_{EI} in Fig. 3. At $J/t = 2.2$, the stationary point is located at $\delta_{EI} = 0$, meaning that there is no symmetry breaking. For larger J, i.e., $J/t = 2.4$ and 2.6, another stationary point appears around $\delta_{\mathrm{EI}} \simeq 0.175$ and 0.26, respectively. In this way, we conclude that the EI phase is realized for $J/t \gtrsim 2.3$. The minimum is always uniquely identified; namely, no double-minimum structure has been observed in the parameter region we have examined.

E. Optical conductivity with vertex correction

We first introduce the current operator j_Λ in the Λ $(= x, y, z)$ direction. In the cluster representation, j_Λ is given by

$$j_\Lambda = i \sum_{\boldsymbol{q}\sigma} \sum_{ll'} c^\dagger_{\boldsymbol{q}l\sigma} v^{ll'}_{\boldsymbol{q}\Lambda} c_{\boldsymbol{q}l'\sigma}, \tag{23}$$

where $\boldsymbol{q}$ denotes the momentum in the reduced Brillouin zone and l is the combined site-orbital index within the cluster (see Sec. III B). The velocity $v^{ll'}_{\boldsymbol{q}\Lambda}$ is given by

$$v^{ll'}_{\boldsymbol{q}\Lambda} = -\sum_{\boldsymbol{R}} e^{-i\boldsymbol{q}\cdot\boldsymbol{R}} (\boldsymbol{\mathcal{T}}_{\boldsymbol{R}})_{ll'} [\boldsymbol{R} - (\boldsymbol{r}_l - \boldsymbol{r}_{l'})]_\Lambda + (\mathcal{H})_{ll'} (\boldsymbol{r}_l - \boldsymbol{r}_{l'})_\Lambda, \tag{24}$$

where the matrices $\mathcal{H}$ and $\boldsymbol{\mathcal{T}}_{\boldsymbol{R}}$ are defined in Eqs. (12) and (14), respectively. The vector $\boldsymbol{r}_l$ represents the position of site i corresponding to index $l \equiv (i, \alpha)$. From the Kubo formula,

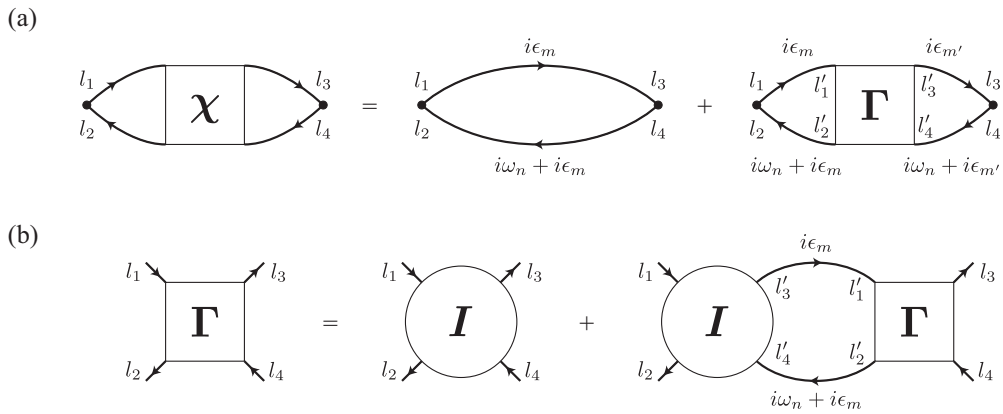

FIG. 4. Diagrammatic representations of (a) the two-particle Green's function $\boldsymbol{\chi}^{\boldsymbol{qq}'}(i\omega_n)$ in Eq. (29) and (b) the Bethe-Salpeter equation for the vertex function $\boldsymbol{\Gamma}(i\omega_n)$ in Eq. (32).

the optical conductivity $\sigma_{\Lambda\Lambda'}(\omega)$ can evaluated by

$$\sigma_{\Lambda\Lambda'}(\omega) = \frac{e^2}{N}\frac{1}{\omega}\mathrm{Im}B_{\Lambda\Lambda'}(\omega + i\eta), \tag{25}$$

where η is an infinitesimally small constant. $B_{\Lambda\Lambda'}(\omega)$ is the current-current correlation function defined by

$$B_{\Lambda\Lambda'}(i\omega_n) = -\int_0^\beta d\tau \langle j_\Lambda(\tau) j_{\Lambda'}\rangle. \tag{26}$$

Replacing j_Λ with Eq. (23), we obtain the explicit expression for $B_{\Lambda\Lambda'}(i\omega_n)$ as

$$B_{\Lambda\Lambda'}(i\omega_n) = \sum_{\boldsymbol{qq}'}\sum_{l_1l_2l_3l_4}\sum_{\sigma\sigma'} v^{l_1l_2}_{\boldsymbol{q}\Lambda}\chi^{\boldsymbol{q}\sigma,\boldsymbol{q}'\sigma'}_{l_1l_2l_3l_4}(i\omega_n)v^{l_4l_3}_{\boldsymbol{q}'\Lambda'}, \tag{27}$$

where

$$\begin{aligned}\chi^{\boldsymbol{q}\sigma,\boldsymbol{q}'\sigma'}_{l_1l_2l_3l_4}(i\omega_n) &= \int_0^\beta d\tau \left\langle c^\dagger_{\boldsymbol{q}l_1\sigma}(\tau)c_{\boldsymbol{q}l_2\sigma}(\tau)c^\dagger_{\boldsymbol{q}'l_4\sigma'}c_{\boldsymbol{q}'l_3\sigma'}\right\rangle \\ &\equiv [\boldsymbol{\chi}^{\boldsymbol{qq}'}(i\omega_n)]_{(\sigma l_1l_2),(\sigma' l_3l_4)}\end{aligned} \tag{28}$$

is the two-particle Green's function. We introduced the matrix notation $\boldsymbol{\chi}^{\boldsymbol{qq}'}$ in the second line to simplify the following descriptions.

We now calculate $\boldsymbol{\chi}^{\boldsymbol{qq}'}(i\omega_n)$ in an approximation which is consistent with the VCA. There are two types of contributions,

$$\boldsymbol{\chi}^{\boldsymbol{qq}'}(i\omega_n) = \delta_{\boldsymbol{qq}'}\boldsymbol{\chi}^{\boldsymbol{q}}_0(i\omega_n) + \boldsymbol{\chi}^{\boldsymbol{qq}'}_{\mathrm{corr}}(i\omega_n). \tag{29}$$

The diagrammatic representation is shown in Fig. 4(a). The first term corresponds to the "bubble" diagram, which is explicitly represented as

$$\begin{aligned}&\left[\boldsymbol{\chi}^{\boldsymbol{q}}_0(i\omega_n)\right]_{(\sigma l_1l_2),(\sigma' l_3l_4)} \\ &\quad = -\delta_{\sigma\sigma'}T\sum_{\epsilon_m}\mathcal{G}^\sigma_{l_3l_1}(\boldsymbol{q}, i\epsilon_m)\mathcal{G}^\sigma_{l_2l_4}(\boldsymbol{q}, i\omega_n + i\epsilon_m),\end{aligned} \tag{30}$$

where ϵ_m is the fermionic Matsubara frequency. The second contribution $\boldsymbol{\chi}^{\boldsymbol{qq}'}_{\mathrm{corr}}$ describes vertex corrections. The full (reducible) vertex Γ, in general, depends on three frequencies and two momenta (the momentum transfer $\boldsymbol{Q}$ is fixed at $\boldsymbol{Q} = 0$), namely, $\Gamma = \boldsymbol{\Gamma}^{\boldsymbol{qq}'}(i\omega_n; i\epsilon_m, i\epsilon_{m'})$. In the VCA, the momentum dependence can be dropped as in the local approximation to the self-energy. Furthermore, we neglect the fermionic frequencies, ϵ_m and $\epsilon_{m'}$, keeping only the bosonic frequency ω_n. This approximation has been adopted in the literature [41,42]. The vertex correction is thus expressed as

$$\boldsymbol{\chi}^{\boldsymbol{qq}'}_{\mathrm{corr}}(i\omega_n) = \boldsymbol{\chi}^{\boldsymbol{q}}_0(i\omega_n)\boldsymbol{\Gamma}(i\omega_n)\boldsymbol{\chi}^{\boldsymbol{q}'}_0(i\omega_n). \tag{31}$$

The vertex part $\boldsymbol{\Gamma}(i\omega_n)$ is represented in terms of the irreducible vertex $\boldsymbol{I}(i\omega_n)$ using the Bethe-Salpeter equation

$$\boldsymbol{\Gamma}(i\omega_n) = \boldsymbol{I}(i\omega_n) + \frac{L}{N}\sum_{\boldsymbol{q}}\boldsymbol{I}(i\omega_n)\boldsymbol{\chi}^{\boldsymbol{q}}_0(i\omega_n)\boldsymbol{\Gamma}(i\omega_n). \tag{32}$$

Figure 4(b) shows the diagrammatic expression of this equation. $\boldsymbol{I}(i\omega_n)$ is the two-particle counterpart of the self-energy and therefore is considered to be local. We compute $\boldsymbol{I}(i\omega_n)$ in the reference system by solving the Bethe-Salpeter equation defined within the cluster.

The above equations are solved once after the variational parameters are fixed by the procedure in Sec. III D. A typical computational time for the calculation of $\sigma_{\Lambda\Lambda'}(\omega)$ is about 5 min, whereas finding the stationary point takes only several seconds.

IV. RESULTS

A. Finite-T phase diagram

First, we calculate the temperature dependences of the order parameters of the AF, EI, and HL states defined by $P_{\mathrm{AF}} = \langle p_{\mathrm{AF}}\rangle$, $P_{\mathrm{EI}} = \langle p_{\mathrm{EI}}\rangle$, and $P_{\mathrm{HL}} = \langle p_{\mathrm{HL}}\rangle$, respectively. The order parameters as a function of J are shown in Fig. 5(a). With increasing J, the LS state realized in $J/t \lesssim 2.3$ is changed into the EI ordered state through the second-order phase transition. This is changed further into the HS state associated with the AF order through the first-order phase transition at $J/t \sim 3.25$. Temperature dependences of the order parameters at $J/t = 2.928$ are shown in Fig. 5(b). With decreasing temperature, a sequential phase transition occurs: the second-order phase transition from the paramagnetic phase to the HL ordered phase at $T/t \sim 0.28$ and the first-order transition to the EI phase at $T/t \sim 0.24$.

Calculated results are summarized in the finite-temperature phase diagram shown in Fig. 6, in which open and solid symbols represent the first- and second-order phase transitions,

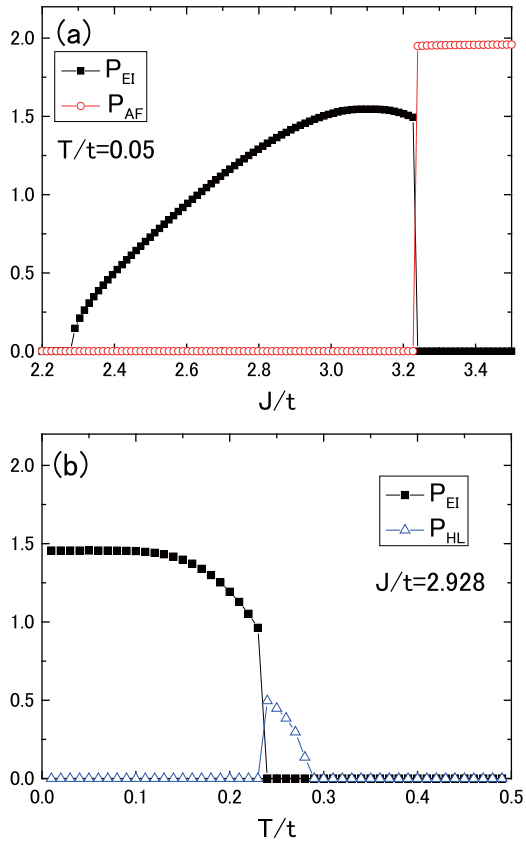

FIG. 5. (a) The order parameters as a function of Hund's coupling at $T/t = 0.005$ and (b) those as a function of the temperature at $J/t = 2.928$.

respectively. In the regions of small and large J/t, the LS and HS states are realized, respectively, as expected from the electronic structures in a single site. Between the two phases, the EI phase appears in low temperatures. The HL ordered phase appears above the EI phase around $2.5 < J/t < 3.0$. In Ref. [15], the finite-temperature phase diagram was obtained by applying the mean-field approximation to the effective pseudospin model derived from the two-orbital Hubbard model. It was shown that the HL phase is realized down to $T = 0$, in contrast to Fig. 6. This difference is attributed to the fact that the spin entropy in the HL phase is overestimated in the mean-field approximation in Ref. [15].

B. One-particle excitation spectra

We calculate the single-particle excitation spectra defined by

$$\rho^{\sigma}(\boldsymbol{k},\omega) = -\frac{1}{\pi}\mathrm{Im}\sum_{\alpha} g^{\sigma}_{\alpha}(\boldsymbol{k},\omega+i\eta), \tag{33}$$

where $g^{\sigma}_{\alpha}(\boldsymbol{k},\omega)$ is the lattice Green's function in the original Brillouin zone for the orbital $\alpha(=a,b)$. Following the CPT [20], we compute $g^{\sigma}_{\alpha}(\boldsymbol{k},\omega)$ from the cluster Green's function $\mathcal{G}^{\sigma}_{ll'}(\boldsymbol{k},\omega)$ by

$$g^{\sigma}_{\alpha}(\boldsymbol{k},\omega) = \frac{1}{L/2}\sum_{l,l'\in\alpha} e^{-i\boldsymbol{k}\cdot(\boldsymbol{r}_l-\boldsymbol{r}_{l'})}\mathcal{G}^{\sigma}_{ll'}(\boldsymbol{k},\omega), \tag{34}$$

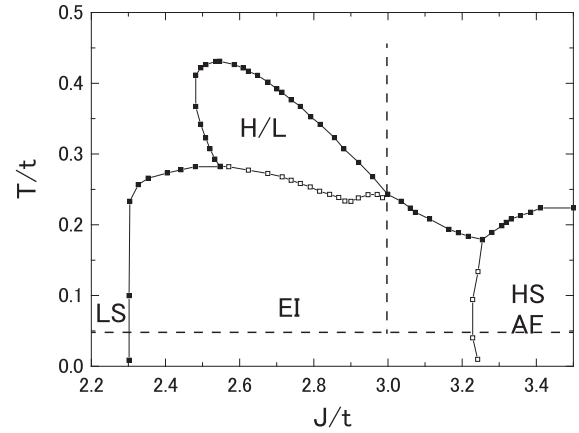

FIG. 6. The finite-temperature phase diagram. Solid and open squares represent the second- and first-order phase transitions, respectively. Horizontal and vertical lines represent the parameter sets adopted in Figs. 8 and 10, respectively.

where the summations for $l \equiv (i,\alpha)$ and $l' \equiv (j,\alpha)$ are taken for all sites in the cluster, keeping the orbital index α. The intensity maps of the spectral functions and the density of states (DOS) at $T/t = 0.05$ are shown in Fig. 7. The ground states for the results in Figs. 7(a), 7(b) and 7(c) are the LS, EI, and HS states, respectively. In the LS state shown in Fig. 7(a), the valence and conduction bands mainly consist of the a and b orbitals, respectively, and the Fermi level is located inside of the band gap. The small component of the b (a) orbital in the valence (conduction) band is induced by the pair-hopping interaction. The dispersion relations are almost reproduced by the noninteracting tight-binding model; that is, the system is a band insulating state. In the EI state shown in Fig. 7(b), the hybridization between the a and b orbitals is realized. The one-particle excitation spectra mainly consist of two parts: cosinelike bands similar to the ones in the LS phase [see Fig. 7(a)] and new bands which appear around M (Γ) points in the valence (conduction) band. The latter is termed shadow bands from now on. The bottom of the conduction band and the top of the valence band are flattened in comparison with the simple cosine bands in the LS state. As a result, the energy gap is enlarged. These characteristics originate from the staggered EI order which corresponds to the band mixing between the top of the valence band around the Γ point and the bottom of the valence band round the M point. In the HS state shown in Fig. 7(c), the hybridization between the two orbitals does not appear. Each orbital band is separated into the upper Hubbard band (UHB) and the lower Hubbard band (LHB), and the Fermi level is located between the LHB for the a orbital and the UHB for the b orbital. That is, the system is identified as a Mott insulating state.

The results in the higher-temperature HL state are shown in Fig. 7(d). The a- (b-) orbital component in the conduction (valence) band is not due to the hybridization effect but mainly due to the HL order and the thermal effect. When we compare the results in Fig. 7(d) with Fig. 7(b), the shadow bands appear only in the EI state. On the other hand, the band structures and DOS in Fig. 7(d) are almost explained by the simple averages of the results in the LS state and the HS state shown in Figs. 7(a) and 7(c), respectively.

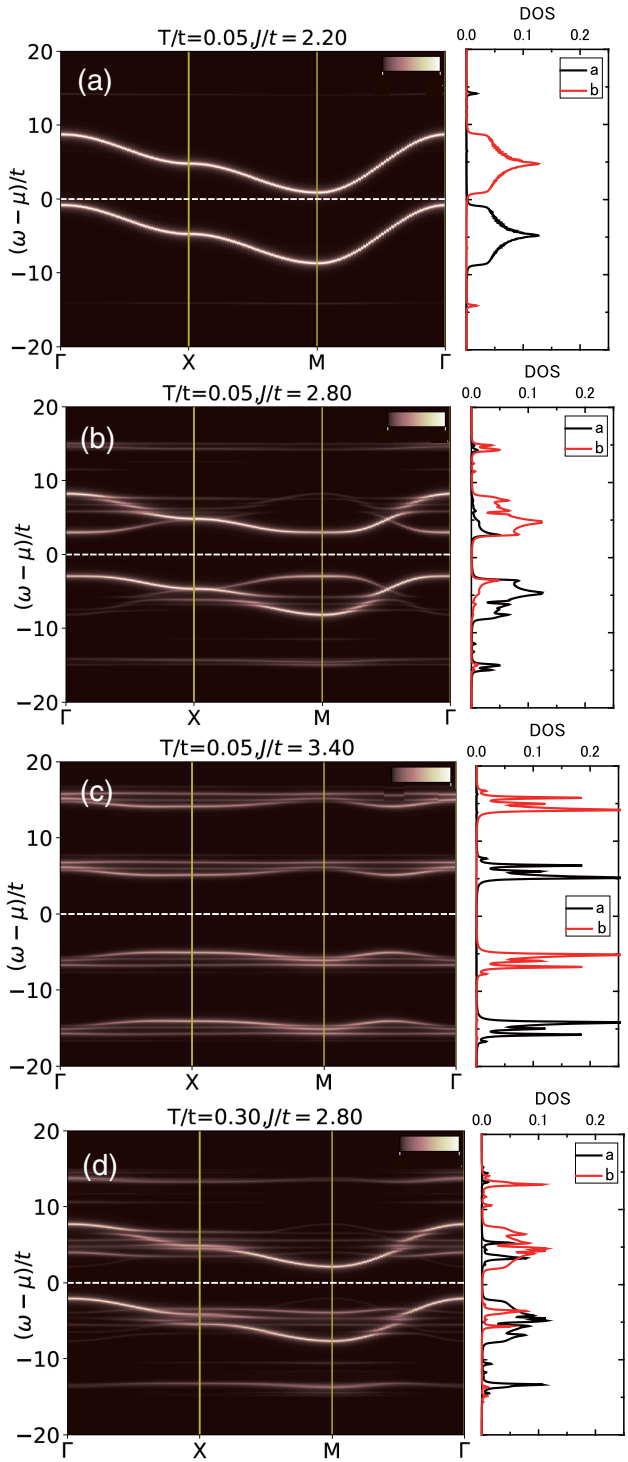

FIG. 7. Intensity plots of the one-particle excitation spectra for (a) $J/t = 2.2$, (b) 2.8, (c) 3.4, and (d) 2.8. We set $T/t = 0.05$ in (a)–(c) and 0.3 in (d), and $\eta = 0.1$. The right panels show the DOS, where black and red lines represent the a and b orbital components, respectively.

C. Optical conductivity spectra

Figure 8 shows the optical conductivity spectra for several values of J/t at $T/t = 0.05$. For comparison, results with and without the vertex corrections are plotted. The vertex

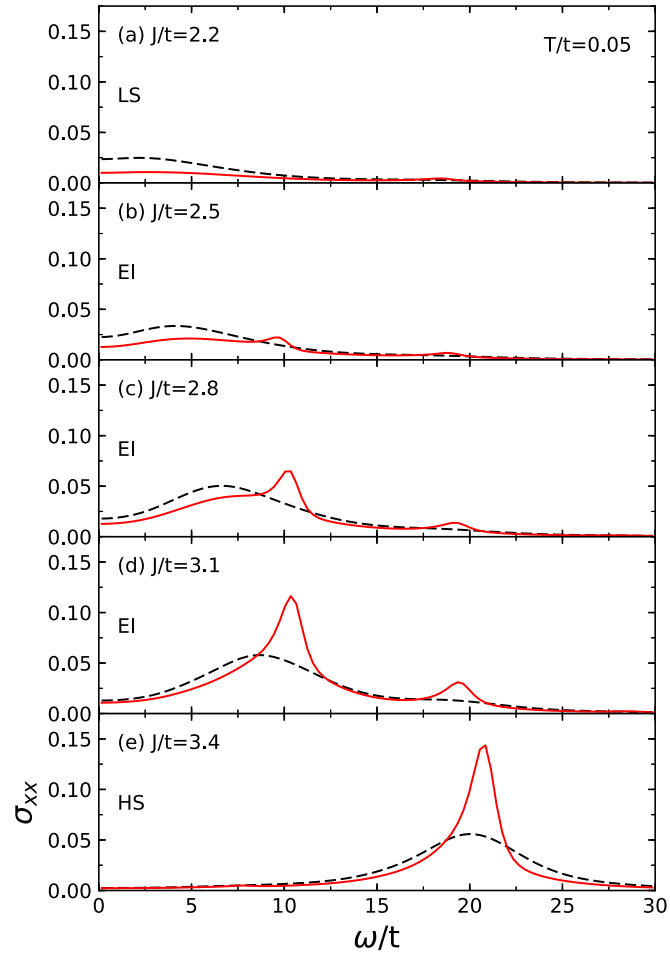

FIG. 8. Optical conductivity spectra for several values of J at $T/t = 0.05$. The red solid lines show results including the vertex corrections, while the black dashed results show results without the vertex corrections [computed only with the first term in Eq. (29)].

corrections incorporate local contributions within the cluster, as shown below. In the LS phase, there are no remarkable peaks in $\sigma(\omega)$, and the total spectral weight is small. This is attributed to the fact that the valence band consists mainly of the b orbital, and there is no electron hopping between the nearest-neighbor a and b orbitals. Weak spectra are caused by the thermal fluctuation and the pair-hopping interaction. In the EI phase, a new peak around $\omega/t \sim 10$ and a continuum around $3 \lesssim \omega/t \lesssim 8$ appear. Since these are related to the EI order as explained below, we term these the EI components from now on. The intensity of the EI component increases with increasing J/t in the EI phase. A small peak around $\omega/t = 20$ exists in the EI phase and changes into a sharp peak in the HS phase, in which the EI component almost disappears. This peak is termed the Hubbard component from now on.

These EI components are attributed to the mixing of the a and b orbitals. Since the wave function in the EI phase is represented by the linear combinations of the LS and HS states, e.g., $C_{\mathrm{L}}|a^0b^2\rangle + C_{\mathrm{H}}|a^1b^1\rangle$ with coefficients C_{L} and C_{H} [see Fig. 9(a)], new optical-excitation processes in the nearest-neighbor sites open. As explained in the previous section, the one-particle excitation spectra shown in Fig. 7(b) mainly

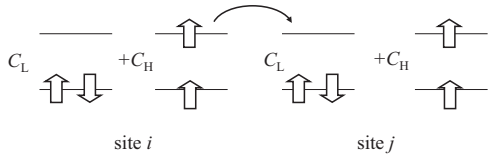

FIG. 9. Schematic optical excitation processes in the EI component. Vertical bars and arrows represent the orbitals and the spin directions, respectively. Symbols C_L and C_H are the coefficients of the wave function in the EI state (see text).

consist of the cosinelike bands and the shadow bands. The sharp EI components around $\omega/t \sim 10$ originate from the transitions between the cosine-type conduction and valence bands. This is prohibited in the LS phase since the a (b) orbitals are almost occupied (unoccupied) and is permitted in the EI phase. Since the two bands almost overlap by the parallel shift of D, the optical excitations between the bands induce the sharp peak structure around $\omega = D$. On the other hand, the continuum in the EI component is attributed to the optical transitions between the cosinelike valence (conduction) band and the shadow conduction (valence) band around the Γ (M) point. These excitations spread from the band gap, which is about $3t$, up to about $10t$. The spectral weight in the EI component is approximately estimated to be $|C_L C_H|^2$. The Hubbard component is identified as the intersite electronic excitation between the nearest-neighbor HS states with the antiferromagnetic spin configuration, and the excitation energy is of the order of U. This excitation is possible even in the EI phase, and the spectral weight is approximately given by $|C_H|^4$.

In Fig. 10, we show the temperature dependence of the optical conductivity spectra at $J/t = 3$, in which the EI state is the ground state and the EI-ordering temperature is $T/t = 0.25$. An overall feature of the optical spectra does not show remarkable changes; the EI component and the Hubbard component exist in the whole temperature range. With increasing temperature from $T/t = 0.05$, the sharp peak around $\omega/t = 10$ becomes remarkable, and the continuum in $3 \lesssim \omega/t \lesssim 8$ is reduced. These behaviors correspond to the one-particle excitation spectra shown in Fig. 7(d), where although the two-orbital components are mixed, the shadow bands in the occupied (unoccupied) band at the M (Γ) points shown in Fig. 8(b) do not appear. This mixing between the two-orbital components originates from the thermal effect through the Boltzmann factor; that is, the local electronic states with the LS and HS configurations are mixed at each site, and the optical excitation between the NN states is realized when the LS and HS states are located in the neighboring sites. The intensity of the EI component is of the order of $(e^{-\beta\Delta E})^2$, where ΔE is the energy difference between the local LS and HS configurations.

We analyze qualitatively the EI component in the optical conductivity spectra. We calculate the integrated intensities of the EI peak defined by $K_{EI} = \int_0^{\omega_c} \sigma_{xx}(\omega) d\omega$. The cutoff frequency is set to $\omega_c/t = 15$, which is located between the EI and Hubbard components. We confirmed that the results do not change much even if ω_c/t is shifted between 12 and 18. Figure 11(b) shows K_{EI} at $T/t = 0.05$ as a function of J. For comparison, the EI order parameter p_{EI} is also presented

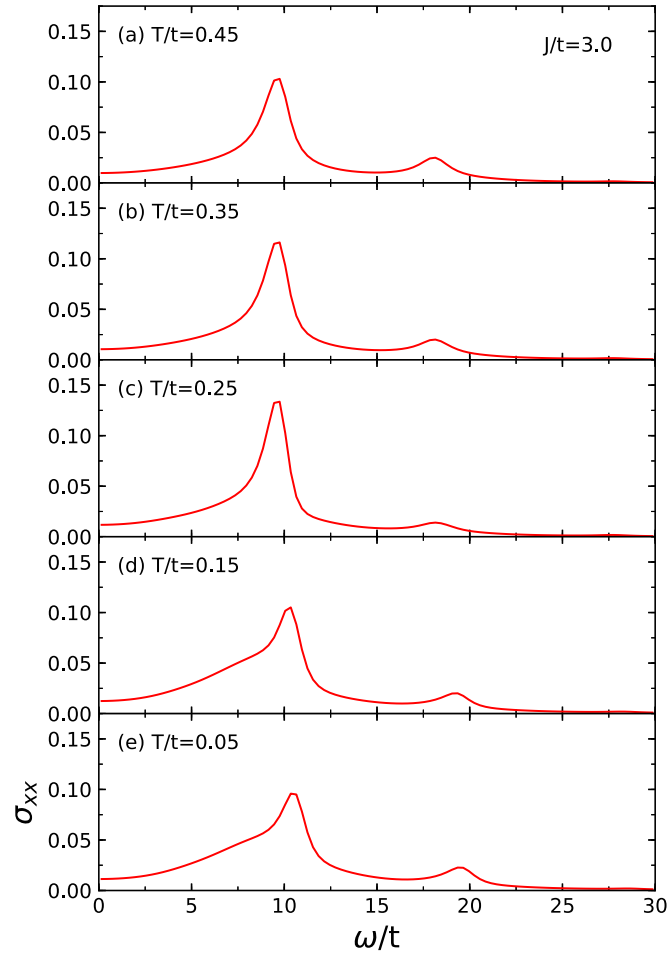

FIG. 10. Optical conductivity spectra for several values of T at $J/t = 3.00$.

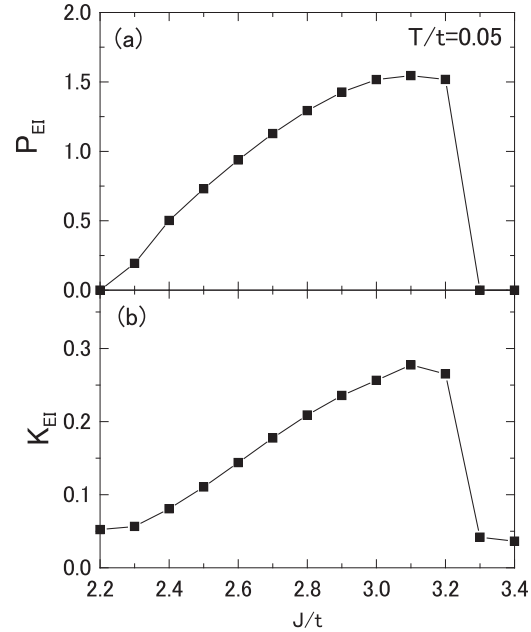

FIG. 11. (a) The EI order parameter p_{EI} and (b) the integrated intensity of the EI component in the optical conductivity spectra K_{EI} as functions of J/t at $T/t = 0.05$.

in Fig. 11(a). Good correspondence is found between $p_{\rm EI}$ and $K_{\rm EI}$, consistent with our explanation that the EI peak appears as a result of the mixing of the two orbitals by the EI order. Finite values of $K_{\rm EI}$ at $J/t = 2.2$ and 3.4 are attributed to η for the analytical continuation. The present analyses demonstrate that the EI peak intensity reflects the EI order parameters in the low-T region and is available to identify the EI state.

V. CONCLUDING REMARKS

In summary, we studied the optical responses in the EI states. The VCA method was applied to the two-orbital Hubbard model with a finite energy difference between the orbitals. In the analyses of the ground state, we considered possibilities of the LS state, the HS-AF state, the EI state, and the HL state. The optical conductivity spectra were formulated by the Green's function method, where the vertex correction is taken into account. We found the characteristic components in the optical spectra attributed to the quantum hybridization of the conduction and valence bands. There is good correspondence between the EI order parameter and the integrated weight of this component at low temperatures. We propose that this component is available to identify the EI state in the real systems.

ACKNOWLEDGMENTS

This work was supported by JSPS KAKENHI Grants No. 15H02100, No. 17H02916, No. 18H05208, No. 18H01158, and No. 18H04301 (J-Physics). The computation in this work was done using the facilities of the Supercomputer Center, the Institute for Solid State Physics, the University of Tokyo.

[1] N. F. Mott, Philos. Mag. **6**, 287 (1961).
[2] J. Zittartz, Phys. Rev. **164**, 575 (1967).
[3] D. Jérome, T. M. Rice, and W. Kohn, Phys. Rev. **158**, 462 (1967).
[4] B. I. Halperin and T. M. Rice, Rev. Mod. Phys. **40**, 755 (1968).
[5] H. Cercellier, C. Monney, F. Clerc, C. Battaglia, L. Despont, M. G. Garnier, H. Beck, P. Aebi, L. Patthey, H. Berger, and L. Forró, Phys. Rev. Lett. **99**, 146403 (2007).
[6] Y. Wakisaka, T. Sudayama, K. Takubo, T. Mizokawa, M. Arita, H. Namatame, M. Taniguchi, N. Katayama, M. Nohara, and H. Takagi, Phys. Rev. Lett. **103**, 026402 (2009).
[7] Y. Tokura, Y. Okimoto, S. Yamaguchi, H. Taniguchi, and T. Kimura, and H. Takagi, Phys. Rev. B **58**, R1699 (1998).
[8] K. Asai, A. Yoneda, O. Yokokura, J. M. Tranquada, G. Shirane, and K. Kohn, J. Phys. Soc. Jpn. **67**, 290 (1998).
[9] S. Tsubouchi, T. Kyômen, M. Itoh, P. Ganguly, M. Oguni, Y. Shimojo, Y. Morii, and Y. Ishii, Phys. Rev. B **66**, 052418 (2002).
[10] S. Tsubouchi, T. Kyômen, M. Itoh, and M. Oguni, Phys. Rev. B **69**, 144406 (2004).
[11] A. Ikeda, T. Nomura, Y. H. Matsuda, A. Matsuo, K. Kindo, and K. Sato, Phys. Rev. B **93**, 220401(R) (2016).
[12] J. Kuneš and P. Augustinský, Phys. Rev. B **89**, 115134 (2014).
[13] J. Kuneš and P. Augustinský, Phys. Rev. B **90**, 235112 (2014).
[14] J. Nasu, T. Watanabe, M. Naka, and S. Ishihara, Phys. Rev. B **93**, 205136 (2016).
[15] T. Tatsuno, E. Mizoguchi, J. Nasu, M. Naka, and S. Ishihara, J. Phys. Soc. Jpn. **85**, 083706 (2016).
[16] Y. F. Lu, H. Kono, T. I. Larkin, A. W. Rost, T. Takayama, A. V. Boris, B. Keimer, and H. Takagi, Nat. Commun. **8**, 14408 (2017).
[17] S. Mor, M. Herzog, D. Golež, P. Werner, M. Eckstein, N. Katayama, M. Nohara, H. Takagi, T. Mizokawa, C. Monney, and J. Stähler, Phys. Rev. Lett. **119**, 086401 (2017).
[18] D. Werdehausen, T. Takayama, M. Höppner, G. Albrecht, A. W. Rost, Y. Lu, D. Manske, H. Takagi, and S. Kaiser, Sci. Adv. **4**, eaap8652 (2018).
[19] M. Potthoff, M. Aichhorn, and C. Dahnken, Phys. Rev. Lett. **91**, 206402 (2003).
[20] D. Sénéchal, D. Perez, and M. Pioro-Ladrière, Phys. Rev. Lett. **84**, 522 (2000).
[21] A. Georges, G. Kotliar, W. Krauth, and M. J. Rozenberg, Rev. Mod. Phys. **68**, 13 (1996).
[22] M. H. Hettler, M. Mukherjee, M. Jarrell, and H. R. Krishnamurthy, Phys. Rev. B **61**, 12739 (2000).
[23] G. Kotliar, S. Y. Savrasov, G. Pálsson, and G. Biroli, Phys. Rev. Lett. **87**, 186401 (2001).
[24] C. Dahnken, M. Aichhorn, W. Hanke, E. Arrigoni, and M. Potthoff, Phys. Rev. B **70**, 245110 (2004).
[25] M. Aichhorn, H. G. Evertz, W. von der Linden, and M. Potthoff, Phys. Rev. B, **70**, 235107 (2004).
[26] D. Sénéchal, P.-L. Lavertu, M.-A. Marois, and A.-M. S. Tremblay, Phys. Rev. Lett. **94**, 156404 (2005).
[27] P. Sahebsara and D. Sénéchal, Phys. Rev. Lett. **100**, 136402 (2008).
[28] S. L. Yu, X. C. Xie, and J. X. Li, Phys. Rev. Lett. **107**, 010401 (2011).
[29] W. Koller and N. Dupuis, J. Phys.: Condens. Matter **18**, 9525 (2006).
[30] E. Arrigoni, M. Knap, and W. von der Linden, Phys. Rev. B **84**, 014535 (2011).
[31] M. Knap, E. Arrigoni, and W. von der Linden, Phys. Rev. B **83**, 134507 (2011).
[32] M. Knap, W. von der Linden, and E. Arrigoni, Phys. Rev. B **84**, 115145 (2011).
[33] F. Hofmann, M. Eckstein, E. Arrigoni, and M. Potthoff, Phys. Rev. B **88**, 165124 (2013).
[34] M. Potthoff, Eur. Phys. J. B **32**, 429 (2003).
[35] M. Potthoff, Eur. Phys. J. B **36**, 335 (2003).
[36] R. Eder, Phys. Rev. B **78**, 115111 (2008).
[37] D. Sénéchal, arXiv:0806.2690.
[38] J. M. Luttinger and J. C. Ward, Phys. Rev. **118**, 1417 (1960).
[39] K. Seki, R. Eder, and Y. Ohta, Phys. Rev. B **84**, 245106 (2011).
[40] T. Kaneko, K. Seki, and Y. Ohta, Phys. Rev. B **85**, 165135 (2012).
[41] T. Sato, K. Hattori, and H. Tsunetsugu, Phys. Rev. B **86**, 235137 (2012).
[42] T. Sato and H. Tsunetsugu, Phys. Rev. B **94**, 085110 (2016).